Mechanics of Materials 148 (2020) 103422

Contents lists available at ScienceDirect

Mechanics of Materials

journal homepage: www.elsevier.com/locate/mechmat

A comparative study between elasto-plastic self-consistent crystal plasticity and anisotropic yield function with distortional hardening formulations for sheet metal forming

Zhangxi Feng[a], Seong-Yong Yoon[b], Jae-Hyun Choi[b], Timothy J. Barrett[a], Milovan Zecevic[a], Frederic Barlat[b], Marko Knezevic[a,*]

[a] Department of Mechanical Engineering, University of New Hampshire, 33 Academic Way, Durham, NH 03824, United States
[b] Graduate Institute of Ferrous Technology, Pohang University of Science and Technology, 77 Cheongam-ro, Nam-gu, Pohang, Gyeongbuk 37673, South Korea

ARTICLE INFO

Keywords:
Polycrystalline material
Numerical algorithms
Finite elements
Deep drawing
AA6022-T4

ABSTRACT

A comparative study between micro- and macro-mechanical constitutive models is carried out while predicting deformation behavior of an aluminum alloy (AA) 6022-T4 during several loading scenarios of increasing complexity including monotonic tension, large strain cyclic deformation, and drawing of a cylindrical cup. The micro-model is a recently developed implicit formulation of the elasto-plastic self-consistent (EPSC) crystal plasticity, which is coupled with the implicit finite element method (FEM) through a user material subroutine in Abaqus. In the coupled formulation, every finite element integration point embeds the implicit EPSC constitutive law that accounts for the directionality of deformation mechanisms and microstructural evolution. The crystallography based EPSC model integrates a dislocation-based hardening law and accounts for inter-granular and slip system level back-stresses, which make it capable of capturing non-linear unloading and the Bauschinger effect. The macro-model is a recently developed anisotropic yield function incorporating distortional hardening using the homogeneous anisotropic hardening (HAH) approach. The model is also implemented as a user material subroutine in Abaqus. Parameters pertaining to the micro and macro models are identified using experimental data from a set of monotonic and cyclic tests performed for AA6022-T4. Additional experimental data for the alloy in terms of flow stress curves, R-value, and anisotropic yield surface evolution are used to verify the models. Finally, the cup drawing simulations are carried out in the FEM using the two constitutive formulations and geometrical changes including the earing profile and sheet thinning/thickening are compared against each other and with experiments to further verify the predictive characteristics of the models. The two formulations and results are discussed in terms of accuracy and computational efficiency.

1. Introduction

The balance of linear momentum governing equations of solid mechanics can be solved numerically using the finite element method (FEM), provided a constitutive law (i.e. a material model) describing an elasto-plastic material behavior under deformation is available (Ardeljan and Knezevic, 2018; Bathe, 1996). The numerical solution to the governing equations is a pair of work-conjugate stress and strain measures for each FE integration point. The accuracy of the solution is primarily driven by the accuracy of the selected material model. As metal forming operations usually impart non-monotonic, multiaxial deformation conditions to forming parts (Barrett and Knezevic, 2020; Hosford and Caddell, 2011; Jahedi et al., 2015; Wagoner et al., 2013; Zare et al., 2016), material models describing the material behavior in simulations of such forming operations must be strain path change sensitive (Knezevic et al., 2013a, 2013b; Li et al., 2002; Poulin et al., 2019b; Zecevic and Knezevic, 2018b). Sophistication of material models scales not only with the applied deformation but also with the microstructural complexity of novel alloys. AA6022-T4 is an aluminum alloy introduced for improving strength and light-weighting of structures (Henn et al., 2017; Hirsch, 2014; Hirsch and Al-Samman, 2013; Miller et al., 2000; Zarei, 2008). Simulations for predicting formed shapes and accompanied springback are essential the optimization of sheet forming processes (Engler and Hirsch, 2002; Rabahallah et al.,

* Corresponding author at: University of New Hampshire, Department of Mechanical Engineering, 33 Academic Way, Kingsbury Hall, W119, Durham, NH 03824, United States.
E-mail address: marko.knezevic@unh.edu (M. Knezevic).

https://doi.org/10.1016/j.mechmat.2020.103422
Received 29 December 2019; Received in revised form 16 March 2020; Accepted 7 April 2020
Available online 15 May 2020

2009; Yoon et al., 2005). Predictive characteristics of such simulations require an experimental verification. The data allowing for a detailed validation of a cup drawing simulation for the alloy have been provided in (Tian et al., 2017).

Crystallographic glide accommodates the plastic deformation of the alloy while inducing anisotropy of the plasticity response by texture and dislocation structure evolution. Moreover, inter- and intra-granular back-stress fields develop contributing to the deformation process, particularly in unloading/reloading. The material typically exhibits nonlinear unloading, while after continuous loading in the opposite direction, the yield stress reduces relative to that at the end of the prior loading. The phenomenon is known as the Bauschinger effect (BE) (Bauschinger, 1886; Cantara et al., 2019; Zecevic et al., 2016b). The hardening rate with the continuation of loading in the reverse direction is also different from that during prior loading (Hasegawa et al., 1975). These deformation phenomena pertaining to the material behavior are governed by the evolution of microstructure and texture.

Macro-mechanical models involving 3D yield functions have been able to represent such material behavior. In particular, the Yld2004-18p yield function (Barlat et al., 2005) incorporated in the FEM predicts 6 and 8 ears on simulated cups after drawing of anisotropic materials (Yoon et al., 2006). However, a large number of model parameters must be fit to an experimental data set to facilitate the representation of the phenomena. In contrast, micro-mechanical models like an elasto-plastic self-consistent (EPSC) crystal plasticity formulation allow for microstructurally-based incorporation of the phenomena since the mechanisms of plastic deformation are considered by such models (Zecevic and Knezevic, 2015). The EPSC model has been coupled with the FEM using a user material (UMAT) subroutine in Abaqus to predict geometry of parts during metal forming (Zecevic et al., 2017; Zecevic and Knezevic, 2017). In the coupled formulation termed FE-EPSC, every finite element integration point embeds the implicit EPSC constitutive law that accounts for the directionality of deformation mechanisms and microstructural evolution.

The present work carries out a detailed comparison between micro- and macro-mechanical constitutive formulations in predicting mechanical behavior of the alloy AA6022-T4 during several loadings including monotonic tension, large strain cyclic deformation, and drawing of a cylindrical cup. Specifically, the micro-model is a recently developed implicit formulation of the EPSC model running within the FEM framework (Zecevic and Knezevic, 2019), while the macro-model is the anisotropic yield function yld2004-18p in conjunction with an update of the homogeneous anisotropic hardening (HAH) approach (Barlat et al., 2011). Parameters pertaining to the models are identified using experimental data from a set of monotonic and cyclic tests performed for AA6022-T4. The calibrated models are then verified by predicting additional flow stress curves, R-value, and anisotropic yield surfaces and finally used to simulate geometrical changes including the earing profile and sheet thinning during drawing of a cylindrical cup. We show that both models are capable of capturing linear followed by non-linear unloading, the BE, and anisotropy in hardening rates as well as the directionally dependent cup height and thinning of the sheet in drawing. The two formulations are discussed in terms of accuracy, practicality, and computational efficiency.

2. Material and experimental data

The material is a 1 mm thick AA6022-T4 sheet provided by (Alcoa). The chemical composition of the alloy is provided in Table 1. In this Al-Si-Mg alloy the content of Si and Mg is balanced to create Mg_2Si precipitates (Jaafar et al., 2012). Supersaturated solution of α forms GP zones, which further transform to β'' needles followed by β' rods and Q' laths, which could finally form large β + Si precipitates (Miao and Laughlin, 1999). These precipitate are barriers to dislocation glide, with the β'' precipitates proving the most effective hardening (Eskin and Kharakterova, 2001). Unlike in artificially aged materials, the naturally aged T4 treated AA6022 contains GP zones and only tiny precipitates. In the modeling framework that follows, size and distribution of the precipitates is not considered explicitly. Considering their size, the effects of precipitates can be embedded in the initial slip resistance for the micro-model, while in the yield function parameters for the macro-model.

Table 1
Composition of AA6022-T4 in wt%.

Si	Fe	Cu	Mn	Mg	Cr	Zn	Ti	Tin	Al
0.90	0.10	0.045	0.053	0.57	0.027	0.016	0.025	<0.02	balance

Microstructure of the alloy has been presented in our earlier works (Barrett and Knezevic, 2019). Grains were characterized as ellipsoids with average 50:34:20 μm dimensions along RD: TD: ND (rolling direction, transverse direction and normal direction), respectively. Pole figures showing texture are shown in Fig. 1. The texture is represented using 220 weighted crystal orientations for simulations based on the procedure presented in (Barrett et al., 2019; Eghtesad et al., 2018; Knezevic and Kalidindi, 2007; Knezevic and Landry, 2015). Measured and compacted pole figures are visually indistinguishable as well as is the predicted mechanical response based on full and compacted textures.

The alloy has been tested in earlier works (Tian et al., 2017; Zecevic et al., 2016c). True stress-true strain response in simple tension has been measured using the ASTM E8 standard along every 15° increments between the TD and RD. At least three specimens were pulled to fracture to ensure the accuracy. As will be shown in the results section, the alloy shows moderate anisotropy from the hardest RD to the softest TD direction. The origin of such behavior has been described in (Zecevic and Knezevic, 2018a). This data is used for calibration of the models.

The R-value (or R-ratio), as a measure of the sheet formability and plastic anisotropy, was inferred from the full-field strain measurements in simple tension using the digital image correlation (DIC) procedure. In this procedure, the through-thickness strain is inferred using the axial strain and the width strain measured by DIC, while the incompressibility was assumed. The strain fields were used until they were approximately uniform in the calculation of the R-value, which is defined as the plastic width-to-thickness strain ratio. The quantity is a strong function of crystallographic texture (Barrett and Knezevic, 2019; Ghosh et al., 2015). The data will be presented in the results section of the paper for multiple loading directions in two ways: (i) R-value versus orientation at 20 MPa of plastic work ensuring an equivalent amount of plasticity among specimens and (ii) R-value versus true strain. This data is used for verification of the models.

In order to calibrate the deformation characteristics pertaining to large strain cyclic plasticity such as non-linear unloading, the BE, and changes in the hardening rates upon load reversal, the response under large strain cyclic deformation along RD was measured. The data will be shown in the results section of the paper.

Finally, cylindrical cup drawing experimental data from (Tian et al., 2017) is used to evaluate predictive characteristics of the models in terms of geometrical features. In this experiment, the cup drawing was performed from a 170 mm diameter cylindrical blank of 1 mm in thickness. The punch was 100 mm in diameter, with a 12 mm radius, while the die opening was 102 mm, with a 6 mm die radius. Appendix A shows a solidworks drawing of the setup. The punch force versus displacement curve was measured during the experiment. Furthermore, a coordinate-measuring machine was used to record the geometry after drawing and springback. A height gauge was used to measure the cup height as a function of orientation from the RD. The cup thickness was recorded in TD and RD using an ultrasonic thickness gauge. The relevant data will be shown in the results section along with the predictions.

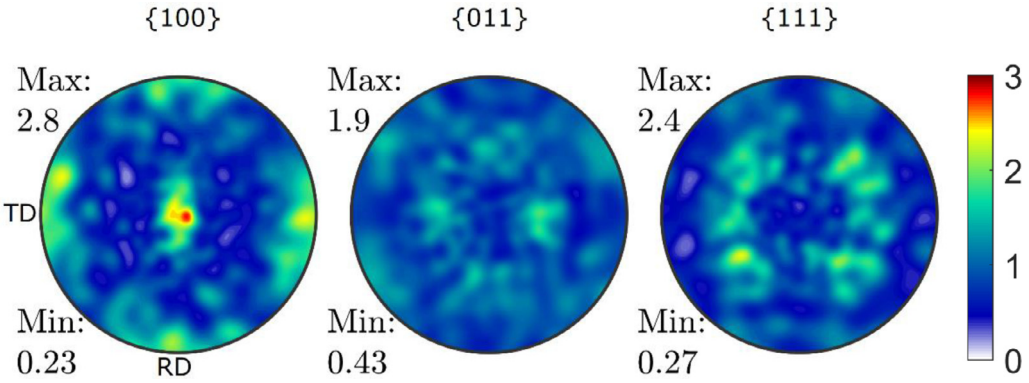

Fig. 1. Pole figures showing the initial texture of AA6022-T4 based on 220 weighted crystal orientations. These orientations are embedded at each integration point for FE-EPSC simulations.

3. Material models

This section summarizes material models for completeness of the work. Specifically, the micro-model is a recently developed implicit formulation of the EPSC model running within the FEM framework (Zecevic and Knezevic, 2019), while the macro-model is the anisotropic yield function yld2004-18p in conjunction with the HAH_{20} hardening approach, an update of the HAH model (Barlat et al., 2011), also running within the FEM framework

3.1. Micro-model (EPSC)

The polycrystalline Jaumann rate of Cauchy stress, $\hat{\boldsymbol{\sigma}}$, and the polycrystalline strain rate, $\dot{\boldsymbol{\varepsilon}}$, are related in EPSC using (Ghorbanpour et al., 2020; Nagtegaal and Veldpaus, 1984; Neil et al., 2010; Zecevic et al., 2015)

$$\hat{\boldsymbol{\sigma}} = \mathbf{L}\dot{\boldsymbol{\varepsilon}} = \cdot\boldsymbol{\sigma} + \boldsymbol{\sigma}\boldsymbol{W} - \mathbf{W}\sigma. \tag{1}$$

Eq. (1) is the same whether a material point is a single crystal or a polycrystalline aggregate. The superposed dot indicates local/Eulerian time derivative. Tensorial quantities, **σ, W**, and **L** are the Cauchy stress, spin, and tangent stiffness, respectively. The same quantities at the crystal level are denoted with the superscript *c* i.e. $\hat{\boldsymbol{\sigma}}^c$, $\dot{\boldsymbol{\varepsilon}}^c$, $\boldsymbol{\sigma}^c$, $\mathbf{W}^c$, and $\mathbf{L}^c$. Starting from the crystal volume average $\hat{\boldsymbol{\sigma}} = <\hat{\boldsymbol{\sigma}}^c>$ and $\dot{\boldsymbol{\varepsilon}} = <\dot{\boldsymbol{\varepsilon}}^c>$, **L** can be evaluated using the standard self-consistent homogenization procedure (Eshelby, 1957; Ghorbanpour et al., 2017; Lipinski and Berveiller, 1989; Neil et al., 2010; Turner and Tomé, 1994). A dot product and a tensor product are denoted with · and ⊗, respectively.

Hooke's law is used at the crystal level

$$\hat{\boldsymbol{\sigma}}^c = \mathbf{L}^c\dot{\boldsymbol{\varepsilon}}^c = \mathbf{C}^c(\dot{\boldsymbol{\varepsilon}}^c - \dot{\boldsymbol{\varepsilon}}^{pl,c}) - \boldsymbol{\sigma}^c tr(\dot{\boldsymbol{\varepsilon}}^c). \tag{2}$$

In Eq. (2), $\mathbf{C}^c$ and $\dot{\boldsymbol{\varepsilon}}^{pl,c}$ are the stiffness tensor and the plastic strain rate per crystal *c*, respectively. The plastic strain is a sum of the products between the sharing rates, $\dot{\gamma}^s$ and Schmid tensors $\mathbf{m}^s = \frac{1}{2}(\mathbf{b}^s \otimes \mathbf{n}^s + \mathbf{n}^s \otimes \mathbf{b}^s)$ defined by the slip system geometry ($\mathbf{b}^s$ - the Burgers vector and $\mathbf{n}^s$ - the slip system normal)

$$\dot{\boldsymbol{\varepsilon}}^{pl,c} = \sum_s \mathbf{m}^s\dot{\gamma}^s. \tag{3}$$

The index, *s*, spans over available slip systems in a grain *c*. The model incorporates a strain-path sensitive dislocation density-based law for the evolution of slip system resistance, τ_c^s, and a slip system level back-stress law to influence the resolved shear stress for activation. These laws along with latent hardening are aimed at predicting the anisotropic mechanical response of the alloy during monotonic loading as well as the particularities pertaining to the load reversal deformation such as non-linear unloading, the BE, and changes in the hardening rates. The model naturally accounts for the inter-granular stresses. Activation per slip system is determined using the two conditions

$$\boldsymbol{\sigma}^c\cdot\mathbf{m}^s - \tau_{bs}^s = \tau_c^s, \tag{4a}$$

$$\hat{\boldsymbol{\sigma}}^c\cdot\mathbf{m}^s - \dot{\tau}_{bs}^s = \dot{\tau}_c^s, \tag{4b}$$

where, τ_{bs}^s is a slip system back-stress governing the kinematic hardening effects (Wollmershauser et al., 2012). The condition 4a implies that the stress state is on the crystal yield surface. The condition 4b implies the consistency providing that the stress state stays on the crystal yield surface (Knockaert et al., 2000; Zecevic et al., 2019). The slip system resistance and back-stress evolve using

$$\dot{\tau}_c^s = \sum_{s'} h^{ss'}\dot{\gamma}^{s'}, \tag{5a}$$

$$\dot{\tau}_{bs}^s = \sum_{s'} h_{bs}^{ss'}\dot{\gamma}^{s'}, \tag{5b}$$

where $h^{ss'}$ and $h_{bs}^{ss'}$ are a hardening matrix consisting of partial derivatives, $h^{ss'} = \frac{\partial\tau_c^s}{\partial\gamma^{s'}}$, and a back-stress matrix consisting of partial derivatives, $h_{bs}^{ss'} = \frac{\partial\tau_{bs}^s}{\partial\gamma^{s'}}$. To evaluate the partial derivatives, the equations for τ_c^s and τ_{bs}^s will be given shortly, while the actual expressions can be found in (Zecevic and Knezevic, 2018a). Next, we summarize the slip resistance and the back-stress laws for defining these partial derivatives.

In the description that follows, *s+* and *s-* are used to define a positive and a negative slip directions for every *s* belonging to a slip family (mode) *α*. Resistance to slip consists of three terms (Knezevic et al., 2014, 2013c; Zecevic et al., 2016a)

$$\tau_c^s = \tau_0 + \tau_{forest}^s + \tau_{debris}, \tag{6}$$

with τ_0 denoting an initial fixed value of slip resistance, while τ_{forest}^s and τ_{debris} are evolving terms with statistically stored forest dislocations and debris dislocations, respectively. τ_0 embeds the contributions from the Peierls stress, solid solution strengthening, initial grain size barrier effect, precipitates, and initial content of dislocations. The remaining two terms are defined as

$$\tau_{forest}^s = b\chi G\sqrt{\sum_{s'} L^{ss'}\rho_{tot}^{s'}} \tag{7a}$$

$$\tau_{debris} = 0.086\, Gb\sqrt{\rho_{deb}}\log\left(\frac{1}{b\sqrt{\rho_{deb}}}\right) \tag{7b}$$

In Eq. (7), *b* is the Burgers vector magnitude ($b = 2.86\ 10^{-10}$ m for Al), χ is an interaction constant (Lavrentev, 1980; Mecking and Kocks, 1981) ($\chi = 0.9$), ρ_{tot}^s is the total density of forest dislocation for the s^{th} slip system, ρ_{deb} is the density of debris dislocation population, *G* is the shear modulus taken to be 26.1 GPa, and $L^{ss'}$ is a latent hardening interaction matrix (Franciosi and Zaoui, 1982; Khadyko et al., 2016) (for coplanar slip systems $L^{ss} = 1$ and for the latent hardening interactions $L^{ss'} = 1.4$ (Kocks and Brown, 1966; Zecevic and

Knezevic, 2018a)).

The total density of forest dislocation consist of

$$\rho_{tot}^{s} = \rho_{for}^{s} + \rho_{rev}^{s^+} + \rho_{rev}^{s^-}, \tag{8}$$

where ρ_{for}^{s} is the forward and $\rho_{rev}^{s^+}$ and $\rho_{rev}^{s^-}$ are the reversible densities of dislocations associated with the s^+ and s^-system directions. These densities of dislocations evolve with shearing as follows (Kitayama et al., 2013; Zecevic and Knezevic, 2019)

$$(\text{If } d\gamma^{s^+} > 0)$$
$$\frac{\partial \rho_{for}^{s}}{\partial \gamma^{s}} = (1-p)k_1\sqrt{\textstyle\sum_{s'} g^{ss'}\rho_{tot}^{s'}} - k_2(\dot{\varepsilon}, T)\rho_{for}^{s}, \tag{9a}$$

$$\frac{\partial \rho_{rev}^{s^+}}{\partial \gamma^{s}} = pk_1\sqrt{\sum_{s'} g^{ss'}\rho_{tot}^{s'}} - k_2(\dot{\varepsilon}, T)\rho_{rev}^{s^+}, \tag{10a}$$

$$\frac{\partial \rho_{rev}^{s^-}}{\partial \gamma^{s}} = -k_1\sqrt{\sum_{s'} g^{ss'}\rho_{tot}^{s'}}\left(\frac{\rho_{rev}^{s^-}}{\rho_0^{s}}\right)^{m}, \tag{11a}$$

$$(\text{If } d\gamma^{s^-} > 0)$$
$$\frac{\partial \rho_{for}^{s}}{\partial \gamma^{s}} = (1-p)k_1\sqrt{\textstyle\sum_{s'} g^{ss'}\rho_{tot}^{s'}} - k_2(\dot{\varepsilon}, T)\rho_{for}^{s}, \tag{9b}$$

$$\frac{\partial \rho_{rev}^{s^+}}{\partial \gamma^{s}} = -k_1\sqrt{\sum_{s'} g^{ss'}\rho_{tot}^{s'}}\left(\frac{\rho_{rev}^{s^+}}{\rho_0^{s}}\right)^{m}, \tag{10b}$$

$$\frac{\partial \rho_{rev}^{s^-}}{\partial \gamma^{s}} = pk_1\sqrt{\sum_{s'} g^{ss'}\rho_{tot}^{s'}} - k_2(\dot{\varepsilon}, T)\rho_{rev}^{s^-}, \tag{11b}$$

with $\rho_{for}^{s}(\gamma^{s}=0) = 10^{11}\ m^{-2}$, $\rho_{rev}^{s^+}(\gamma^{s}=0) = 0$ and $\rho_{rev}^{s^-}(\gamma^{s}=0) = 0$. In the above expressions, k_1 is a fitting parameter controlling the rate of dislocation generation, while k_2 is calculated as a rate-sensitive term controlling dynamic recovery of dislocations (Beyerlein and Tomé, 2008), p is a reversibility parameter in the range from 0 to 1, $g^{ss'}$ is an interaction matrix (Khadyko et al., 2016; Kocks et al., 1991; Teodosiu and Raphanel, 1991), m is a parameter controlling the rate of recombination of dislocations (the value is set to 0.5 (Wen et al., 2015)), and ρ_0^{s} is the total density of dislocation at the local path reversal on the system, s^{th} (Kitayama et al., 2013).

The rate-sensitive term, k_2, is calculated using

$$\frac{k_2}{k_1} = \frac{\chi b}{g}\left(1 - \frac{k_B T}{Db^3} ln\left(\frac{\dot{\varepsilon}}{\dot{\varepsilon}_0}\right)\right), \tag{12}$$

with the Boltzmann constant, k_B, a reference strain rate, $\dot{\varepsilon}_0 = 10^7$, a drag stress, D, and an effective activation enthalpy, g. The debris density of dislocation is incremented using

$$\sum_{s}\frac{\partial \rho_{deb}}{\partial \gamma^{s}}d\gamma^{s} = \sum_{s} qb\sqrt{\rho_{deb}}\ k_2(\dot{\varepsilon}, T)\rho_{tot}^{s}d\gamma^{s}, \tag{13}$$

with a fitting parameter for the rate of dislocation recovery, q.

Next, we turn our attention to a back-stress law for defining the back-stress matrix, $h_{bs}^{ss'}$. Back-stress has intra-granular and inter-granular sources in polycrystalline metals governing primarily the BE and unloading characteristics of deformation behavior. Interactions between individual grains of different crystal orientation as well as any presence of incompatibility between hard regions of dislocation cell walls and soft regions of cell interiors within grains give rise to back-stress in polycrystals (Kassner et al., 2013; Mughrabi, 1983). A harder grain surrounded by softer grains will undergo lower plastic deformation than its surrounding neighbors. Incompatibility of accommodated plastic strain between the grains causes accumulation of dislocations around the strong grain, which results in the plastic strain gradient. The dislocations creating the gradient are referred to as the geometrically necessary dislocations (GNDs) (Bayley et al., 2006; Fleck et al., 1994). The built up of back-stress acts against the applied stress during forward loading (Withers and Bhadeshia, 2001). Upon loading in the reverse direction, the applied stresses combine with the back-stress, which results in a drop of the reverse yield stress. While the EPSC model accounts for the elastic interactions between the individual inclusions and HEM, the intra-granular sources at the slip system level are modeled using a phenomenological back-stress law mimicking the physics of its origin. In particular, we consider an evolution law for back-stress per slip system based on the work presented in (Beyerlein and Tomé, 2007; Zecevic et al., 2016b). The slip system sources of back-stress evolve with shear strain. All sources of back-stress on individual slip systems are superimposed to form the back-stress tensor as proposed in (Harder, 1999). The back-stress tensor is then projected on individual slip systems to arrive to the final expression of back-stress. The expression for back-stress on a slip system, τ_{bs}^{s}, is

$$\tau_{bs}^{s} = \mathbf{m}^{s}\cdot\boldsymbol{\sigma}_{bs}^{c} = \tau_{bs,sys}^{s} + 2\sum_{s'}\mathbf{m}^{s}\cdot\mathbf{m}^{s'}\tau_{bs,sys*}^{s'}, \tag{14}$$

where

$$\tau_{bs,sys*}^{s'} = \begin{cases}\tau_{bs,sys}^{s'} \ if\ \ \tau_{bs,sys}^{s'} > 0\\ 0 \ if\ \ \tau_{bs,sys}^{s'} < 0\end{cases}. \tag{15}$$

In Eq. (14), $\boldsymbol{\sigma}_{bs}^{c}$ is the back-stress tensor based on the contribution from the slip system level sources over s' when $s' \neq s$.

The slip system level back-stress is

$$(\text{if } d\gamma^{s^+} > 0 \ \text{ and } \tau_{bs,sys}^{s^+} > 0)$$
$$\tau_{bs,sys}^{s^+} = \tau_{bs}^{sat}(1 - \exp(-\nu\gamma^{s^+})), \tag{16}$$

$$\tau_{bs,sys}^{s^-} = -A\tau_{bs,sys}^{s^+}, \tag{17}$$

$$(\text{if } d\gamma^{s^+} > 0 \text{ and } \tau_{bs,sys}^{s^+} < 0)$$
$$\tau_{bs,sys}^{s^+} = -(A+1)\tau_{bs}^{sat}\exp\left(-\frac{\gamma^{s^-}}{\gamma_b}\right) + \tau_{bs}^{sat}, \tag{18}$$

$$\tau_{bs,sys}^{s^-} = -\frac{1}{A}\tau_{bs,sys}^{s^+}. \tag{19}$$

The fitting constants for the back-stress law are a saturation value, τ_{bs}^{sat}, a parameter governing an asymmetric evolution in $s+$ and s-, A, the denominator, γ_b, and a multiplier, ν. A is a calibration constant enabling an asymmetric evolution of back-stress in $s+$ and s-. The constant provides more flexibility to capture the macroscopic data. For example, the deformation of individual single crystals may results not only from the resolved shear stress along the direction of slip but also from shear stresses resolved along directions orthogonal to the slip direction as well as the three normal stress components inducing asymmetry in back-stress. The shearing strain, γ^{s}, is a value measured relative to the latest load reversal.

To complete the theory, crystal lattice reorientation for texture evolution must be defined. The rate of crystal spin is

$$\mathbf{W}^{c} = \mathbf{W}^{c,app} - \mathbf{W}^{pl,c}, \tag{20}$$

with an applied spin $\mathbf{W}^{c,app}$ and a plastic spin $\mathbf{W}^{pl,c}$. The latter is $\mathbf{W}^{pl,c} = \sum_{s}\dot{\gamma}^{s}\mathbf{q}^{s}$, with $\mathbf{q}^{s} = \frac{1}{2}(\mathbf{b}^{s}\otimes\ \mathbf{n}^{s} - \mathbf{n}^{s}\otimes\ \mathbf{b}^{s})$.

In the brief summary of FE-EPSC that follows, the subscript *FE* denotes quantities passed to or returned from the FEM software. Every FE integration point embeds initially the same 220 weighted crystal orientations. The EPSC constitutive law computes stress at the end of each strain increment, $\boldsymbol{\sigma}_{FE}^{t+\Delta t}$, for a given increment in total strain, $\Delta\boldsymbol{\varepsilon}_{FE}$. The total strain is determined by the applied boundary conditions imposed to an FE mesh. At the end of the increment this quantity is

$$\boldsymbol{\varepsilon}_{FE}^{t+\Delta t} = \boldsymbol{\varepsilon}_{FE}^{t} + \Delta\boldsymbol{\varepsilon}_{FE}. \tag{21}$$

This strain, $\boldsymbol{\varepsilon}_{FE}^{t+\Delta t}$, is accommodated by the EPSC constitutive law for each FE integration point to calculate $\boldsymbol{\sigma}_{\mathrm{FE}}^{t+\Delta t}$ for the Abaqus FE solver. In

addition to Cauchy stress, the implicit FEM solver requires a Jacobian matrix, $\frac{\partial \Delta \boldsymbol{\sigma}_{FE}}{\partial \Delta \boldsymbol{\varepsilon}_{FE}}$, for a new estimate in the displacement field. This derivative is (Zecevic and Knezevic, 2019)

$$\frac{\partial \Delta \boldsymbol{\sigma}_{FE}}{\partial \Delta \boldsymbol{\varepsilon}_{FE}} = \frac{\partial (\boldsymbol{\sigma}_{FE}^{t+\Delta t} - \boldsymbol{\sigma}_{FE}^{t})}{\partial \Delta \boldsymbol{\varepsilon}_{FE}} = \frac{\partial \Delta \overline{\boldsymbol{\sigma}}}{\partial \Delta \overline{\boldsymbol{\varepsilon}}} = \frac{\partial (\overline{\mathbf{L}}^{inc} \Delta \overline{\boldsymbol{\varepsilon}})}{\partial \Delta \overline{\boldsymbol{\varepsilon}}} = \overline{\mathbf{L}}^{inc}, \tag{22}$$

where $\overline{\mathbf{L}}^{inc}$ is the tangent stiffness relating the increments in strain and Cauchy stress. The bar denotes that a variable is in the configuration at the beginning of time increment with respect to the crystal rotation, i.e. the crystal orientation is not updated with the crystal spin acting during the current time increment.

3.2. Macro-model (HAH)

In sheet metal forming simulations, plasticity is traditionally described using an anisotropic yield condition of the type $\bar{\phi} = \sigma_r(\bar{\varepsilon})$, where $\bar{\phi}$ is an effective stress associated with the work-conjugate effective strain $\bar{\varepsilon}$, and $\sigma_r(\bar{\varepsilon})$ a reference flow curve, not necessarily uniaxial tension. This approach has been successful for a number of simulations, in particular, when the deformation is monotonic or pseudo-monotonic. However, when the material is subjected to abrupt strain path changes such as strain reversal, the Bauschinger and transient hardening effects cannot be captured accurately. In order to account for non-linear strain path effects on the material response, kinematic hardening and distortional plasticity approaches are necessary in the context of macroscopic continuum modeling. The homogenous anisotropic hardening (HAH) model is one of such models based on distortional plasticity but without a back-stress (no kinematic hardening). The HAH model was developed to distort any anisotropic yield condition when the strain path changes while, for monotonic loading, to provide the same material response as if the assumption of isotropic hardening was employed.

Recently, a modified version of the homogenous anisotropic hardening model called HAH_{20} (Barlat et al., 2020), was proposed

$$\bar{\sigma}(\mathbf{s}, f_-, f_+, \hat{\mathbf{h}}) = \{\bar{\xi}(\mathbf{s})^q + \phi_h(\mathbf{s}, f_-, f_+, \hat{\mathbf{h}})\}^{\frac{1}{q}} = \sigma_R(\bar{\varepsilon}) \tag{23}$$

where $\mathbf{s}$ is the stress deviator, q a coefficient, and f_-, f_+ and $\hat{\mathbf{h}}$ are three state variables. $\bar{\xi}$ and σ_R are the effective and reference flow stresses that respectively reduce to $\bar{\phi}$ and σ_r mentioned above for monotonic loading. When reverse loading occurs, ϕ_h is the function that describes the amount of distortion and $\hat{\mathbf{h}}$, the so-called microstructure deviator, controls the distortion orientation. $\bar{\xi}$ contains other state variables that affect the material response when cross-loading occurs. Cross-loading is a change such as two uniaxial tension steps with about 60° between the two longitudinal directions that is, when new slip systems are activated. In the HAH framework, it is assumed that any strain path change affects the material constitutive response by a combination of the effects due to reverse loading and cross-loading only.

In the present work, the amount of distortion due to reverse loading ϕ_h, as compared with isotropic hardening, is defined as

$$\phi_h(\mathbf{s}, f_-, f_+, \hat{\mathbf{h}}) = f_-^q \left| \hat{\mathbf{h}} \cdot \mathbf{s} - |\hat{\mathbf{h}} \cdot \mathbf{s}| \right|^q + f_+^q \left| \hat{\mathbf{h}} \cdot \mathbf{s} + |\hat{\mathbf{h}} \cdot \mathbf{s}| \right|^q \tag{24}$$

The yield function $\bar{\phi}$ corresponds to Yld2004-18p (Barlat et al., 2005), which is valid for a general stress state, and the reference flow curve is described by (Hockett and Sherby, 1975) relationship

$$\sigma_r(\bar{\varepsilon}) = \sigma_s - (\sigma_s - \sigma_y)\exp(\bar{\varepsilon}^{\,\eta}/\varepsilon_\eta) \tag{25}$$

where the saturation stress σ_s, the yield stress σ_y, ε_η and η are material coefficients. There are 16 independent anisotropy coefficients in Yld2004-18p (16 independent out of total 18 parameters, as described in (van den Boogaard et al., 2016)) and four hardening coefficients in Hockett-Sherby, which are all determined in a standard fashion before the distortion is considered, that is, using the results of monotonic loading experiments. Yld2004-18p requires the use of an optimization algorithm and Hockett-Sherby of a least-square approximation. These coefficients are determined only once.

An additional feature was added in HAH_{20}, namely, the influence of the hydrostatic stress on plastic flow as demonstrated by (Spitzig et al., 1975). This effect, although small, can lead to substantial strength-differential (S-D) effect in metals and can affect the modeling of tension-compression load cycles. Therefore, the approach proposed by Richmond and Spitzig (1980) was adapted to the present constitutive description, using an overall effective stress $\bar{\Sigma}$ defined as

$$\bar{\Sigma}(\boldsymbol{\sigma}) = \bar{\sigma}(\boldsymbol{\sigma}) + \alpha c I_1(\boldsymbol{\sigma}) = c \tag{26}$$

with the stress tensor $\boldsymbol{\sigma}$ and the function c given by

$$c = \frac{\sigma_r(\bar{\varepsilon})}{1 - \alpha I_1(\boldsymbol{\sigma}^r)} \tag{27}$$

In the last two equations, $\bar{\sigma}$ and σ_r were already defined, $\boldsymbol{\sigma}^r$ is the stress tensor associated with the flow stress σ_r, $I_1(\boldsymbol{\sigma}^r)$ the first invariant of $\boldsymbol{\sigma}^r$ and α the pressure coefficient. α was measured for a number of metals and takes values between 15 and 50 TPa^{-1} (Richmond and Spitzig, 1980).

All the HAH coefficients are optimized after the yield function and the hardening curve are completely identified. Some state variables in HAH_{20} that describe specific effects were not introduced here for the sake of simplicity, in particular, those corresponding to permanent softening, latent hardening and cross-loading contraction. However, the reader is referred to the original paper (Barlat et al., 2020) for more details about these variables and to Yoon et al. (2020) for the finite element implementation of HAH_{20}. In the present work, only the Bauschinger effect and permanent softening are accounted for, which reduces the number of necessary coefficients to only five. The influence of the hydrostatic pressure on plastic flow was also considered in this work by fixing the value of α to 20 TPa^{-1}.

4. Results

This section presents modeling results, starting with the calibration and verification of the models with experimental data followed by an application case study of cup drawing.

4.1. Calibration and verification

In EPSC modeling, a polycrystalline aggregate is represented by a statistically significant set of weighted crystal orientations having ellipsoidal geometries. In the case of the AA6022-T4 sheet, 220 grains were used. Every grain is treated as an elasto-plastic inclusion within the homogeneous-equivalent-medium (HEM) representing the overall properties of the polycrystalline aggregate.

Calibration and verification of the models are performed using a one element model in Abaqus. The model is one linear element C3D8 (continuum 3D 8-nodal) undergoing a simple tension/compression boundary conditions, i.e. displacement along the loading direction and stress-free laterally.

The models are calibrate using monotonic and cyclic data for AA6022-T4. The parameters for both models are adjusted to achieve a good approximation of the experimental data as well as to achieve a good match between the model predictions, as shown in Figs. 2 and Fig. 3. Tables 2 and 3 present the parameters pertaining to the hardening law and the back-stress law in EPSC, while table 4 presents the parameters for the HAH_{20} model. Derails pertaining to calibration procedures have been described in earlier works, in e.g. (Eghtesad and Knezevic, 2020) for the dislocation density-based hardening law and in (Barlat et al., 2005, 2020) for the macro-scale model. For the macro-model, isotropic hardening is fitted first using the monotonic tension data, followed by fitting of the yield function for anisotropy using a procedure presented in (Barlat et al., 2005). The HAH_{20} model parameters are fitted last with the procedure described in (Barlat et al., 2020). Here, the BE and permanent softening effects are accounted for

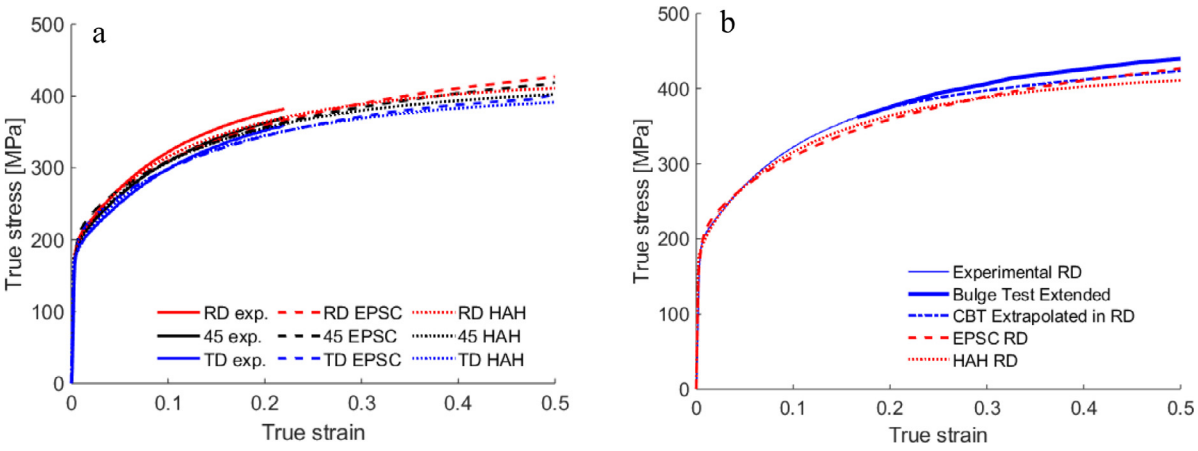

Fig. 2. (a) Comparison of measured (exp.) and simulated true stress-true strain curves along three sample direction as indicated in the legend under a strain rates 0.001 s^{-1} at room temperature. The simulations were performed using FE-EPSC and HAH on one C3D8 element model to a greater strain level than the measured data. (b) Comparison of simulated curves along RD from (a) with the extrapolated curve using the bulge test (Barlat et al., 2002) and the CBT-FEM method (Poulin et al., 2019a). The latter method facilitates the extrapolation along a particular sample direction.

based on the load reversal data. Significantly, the models reproduce anisotropic hardening along the RD, TD, and 45° directions seen experimentally. As the strain levels during drawing are expected to exceed the onset of necking in a simple tension test, the curves are extrapolated using the experimental data based on the bulge test and continuous bending under tension testing (Barlat et al., 2002; Poulin et al., 2019a). Moreover, the models capture the nonlinear unloading, the BE, and changes in the hardening rates during load reversal.

Fig. 3 also shows the predictions of R-value versus strain and versus orientation. Evidently, the magnitude and trends are captured by both models. The figure also shows uniaxial tensile flow stress at a plastic work 20 MPa normalized by the value along RD versus the angle from RD in increments of 15°. Finally, the iso-shear contours at 20 MPa of plastic work are predicted well, with slightly better predictions by the EPSC model. The adjusted models are used to simulate drawing of a cylindrical cup, as will be presented in the next section.

4.2. Predictions

We begin by summarizing the simulation setup, which is consistent with the setup used in (Barrett and Knezevic, 2019). Fig. 4 illustrates the simulation setup along with the FE mesh used to model the drawing of the cylindrical cup. The setup includes the blank, a blank holder, a die and a punch. As the rolled blank exhibits the orthotropic symmetry, the setup is a quarter model with the mirror symmetry imposed in the TD and RD of the blank. The punch, blank holder, and die were modeled as analytically rigid objects. The reduced integration elements, C3D8R, were used for the blank as the fully integrated C3D8 elements can suffer from volumetric and shear locking in bending and are 8 times more computationally intensive. The FE mesh for the blank contained a total of 14,564 elements with 4 elements through thickness. Mesh sensitivety study was performed to converge for the in-plane element dimensions of 1.25 mm in the radial direction, while the element size varies circumferentially. Rows of elements converge to tri/wedge elements at the blank center, which is expected to experience the least amount of plastic deformation. Coulomb friction was used in the simulations. The coefficient of friction was set to $\mu = 0.1$.The simulations were performed using both hard and soft contact conditions and similar results were obtained. It is also observed that increasing the coefficient of friction results in taller and thinner cups requiring larger forming forces. The blank holder was modeled with some compliance to better resemble the experimental setup. During drawing, the rim region of the cup thickens causing the blank holder to lift off. To this end, a spring with a stiffness of 1.25×10^6 N/mm was attached to the holder. After drawing, the springback is simulated by removing the contact constraints and fixing the center node. The cup re-equilibrates in two steps. In the first step, a damping coefficient of 0.02 is used to prevent excessive deformation, while in the second step a damping coefficient of 2×10^{-4} is used for relieving any remaining residual stress.

R-value is an important property of a sheet governing the cup height during forming.The earing profile at the end of drawing can be estimated using (Yoon et al., 2006)

$$h(\theta) = r_p - (r_c - r_b) + \frac{R_{\theta+90}}{R_{\theta+90}+1}((r_c - r_b) + r_b \ln\left(\frac{r_b}{r_c}\right)). \tag{28}$$

In Eq. (28), $h(\theta)$ is the cup height at a given θ from RD, r_b is the radius of the blank, r_c is the radius of the die opening, r_p is the radius of the punch profile, and $R_{\theta+90}$ is the R-value at 90° from the given θ. Fig. 5 shows these results based on the data presented in Fig. 3b. These calculations suggest that the models should be able to predict cup height during forming.

A photo of the cylindrical cup after forming experimentally is shown in Fig. 6. The figure qualitatively compares the photo and simulated cups using the models. The earing formed around the cup rim in simulations resemble those observed in the experiment.

Fig. 7a shows the comparison between measured and predicted punch force versus displacement curves. After approximately 18 mm of the displacement, the cup thickens while the blank holder lifts off resulting in a change of the curvature. The cup is drawn after about 50 mm displacement. The evolution of plastic strain contours and underlying work hardening under the complex mechanical fields during drawing is influenced by texture evolution in EPSC making the response more compliant with strain, while the HAH model remains stiffer imparting higher strain levels for a given punch displacement (Fig. 8). As a result, the punch force predicted by the HAH model is higher than that predicted by the EPSC model. Thinning of the cup is slightly over predicted by the HAH model, while slightly under predicted by the EPSC model. Fig. 7b shows a comparison in the thinning of the cup measured from the center to the rim along TD and RD. The plot is normalized by the total distance. These predictions also show that the HAH model imparts more strain for a given punch displacement than the EPSC model. As is evident, there is slightly more thinning in the TD than the RD, which is associated with the difference in the magnitude of the R-value along TD (smaller) from that along RD (larger). Due to complex distribution of mechanical fields in the sheet during drawing, the R-value, as a measure of the sheet formability defined directionally in uniaxial tension, does not completely describe such thinning behavior but partially and only for the axial component of the fields.

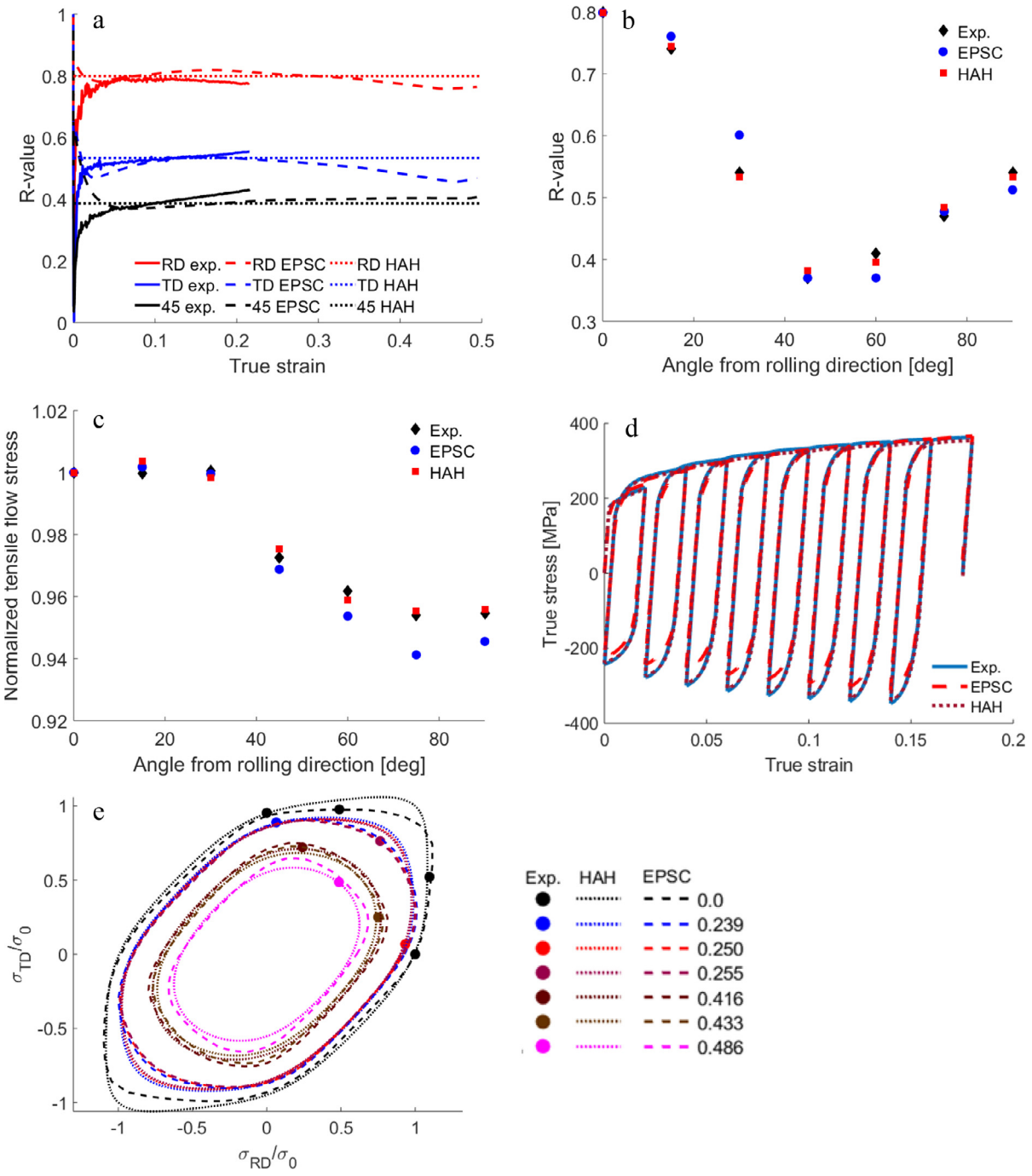

Fig. 3. Comparison of experimentally (exp.) measured and simulated using EPSC and HAH: (a) R-value versus true strain, (b) R-value for 20 MPa plastic work versus the angle from RD in increments of 15°, (c) uniaxial tensile flow stress at a plastic work 20 MPa normalized by the value along RD versus the angle from RD in increments of 15°, (d) large strain cyclic response along RD with a strain amplitude of 0.02 and a mean strain increase of 0.02 per cycle to failure (i.e., 0 – 0.02 – 0 – 0.04 – 0.02 – 0.06 – 0.04 – 0.08 – 0.06 – etc.), and (e) iso-shear contours for 20 MPa plastic work normalized by the yield stress along RD (σ_o). The numbers in the legend of (e) indicate the shear stress at 20 MPa plastic work divided by the σ_o.

Table 2
Fitting parameters for the evolution of slip system resistance for {111} < 1$\bar{1}$0> slip mode in EPSC.

τ_0 [MPa]	k_1	g	D [MPa]	q
56	$5 \cdot 10^7$	0.025	100	4

Table 3
Fitting parameters for the evolution of slip system back-stress in EPSC.

τ_{bs}^{sat} [MPa]	v	γ_b	A
12	560	0.001	0.01

Table 4
Fitting parameters for the macro-model.

Hockett-Sherby									
σ_s[MPa]		σ_y[MPa]		$1/\varepsilon_\eta$	η				
429.9		174.3		4.676	0.7369				
Yld2004-18p									
a		c'_{12}	c'_{13}	c'_{21}	c'_{23}	c'_{31}	c'_{32}	c'_{44}	c'_{55}
8		1	1	0.4396	0.4322	0.7910	1.1356	1.0723	1.0599
c'_{66}		c''_{12}	c''_{13}	c''_{21}	c''_{23}	c''_{31}	c''_{32}	c''_{44}	c''_{55}
0.3736		1.4533	1.1995	0.9938	1.1294	1.0336	1.0901	0.8794	0.8921
c''_{66}									
1.3795									
HAH_{20}									
q	p	k	k'		ξ_r	k_1	k_2	k_3	ξ_b
3	3	250.0	125.0		8.0	250.0	50.0	0.3	4.0
ξ'_b	k_4	k_5	k_S		C	k_C	k'_C	L	k_L
1.5	0.9	15.0	250.0		1.0	50.0	250.0	1.0	500.0
ξ_L	α [TPa^{-1}]								
0.25	20								

Additionally, sheet thickening occurs in the rim area, as is evident from the figure (Fig. 7b). The rim is the last portion of the material that flows from the flat blank (between die and blank-holder) into the wall of the cup. The rim experiences compression acting in the circumferential (hoop) direction. Given that this compression promotes the equivalent anisotropy to that in tension (with more thinning in a given direction under tension is equivalent to more thickening in the same direction under compression), slightly more thickening occurs in the TD. The circumferential compression in TD is in the sheet RD direction. Thus, slightly more thickening of the blank occurs in the RD, while slightly more thinning is in the TD. Fig. 7c and d show a comparison of the earing profiles. Such predictions can determine the portion of cup needing to be trimmed. The peak to valley difference experimentally is about 2.4 mm, while the EPSC model slightly over predicts and the HAH model slightly under predicts the cup height. The difference in strain levels accumulated by the models is also evident here from the total cup heights.

The strain contours after drawing and stress contours before and after springback predicted by the models are compared in Figs. 8 and 9, respectively. While the predicted trends are similar, the HAH model predicts a slightly higher strain and stress as well as the cup a bit thinner. While both models reveal a significant amount of stress relaxation and springback, the higher stress predicted by the HAH model is expected to lead to a slightly larger amount of springback as compared with the EPSC model.

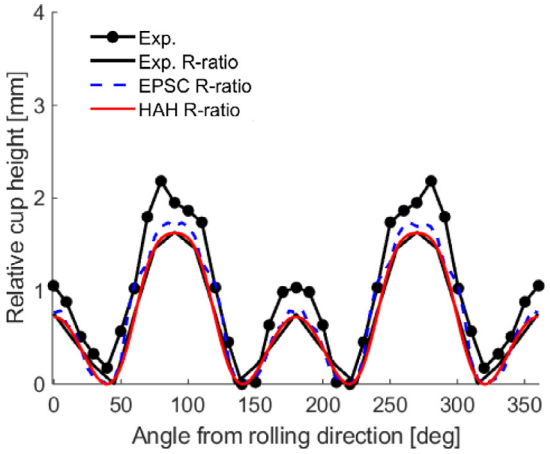

Fig. 5. Cup height based on the R-values from Fig. 3b using Eq. (28) versus the angle from RD along with the experimental data.

5. Discussion

This work used two classes of plasticity models capable to simulate deformation characteristics of AA6022-T4 sheet, one based on the crystal plasticity theory and another based on the continuum plasticity theory. The former model is an EPSC formulation linking the grain-level

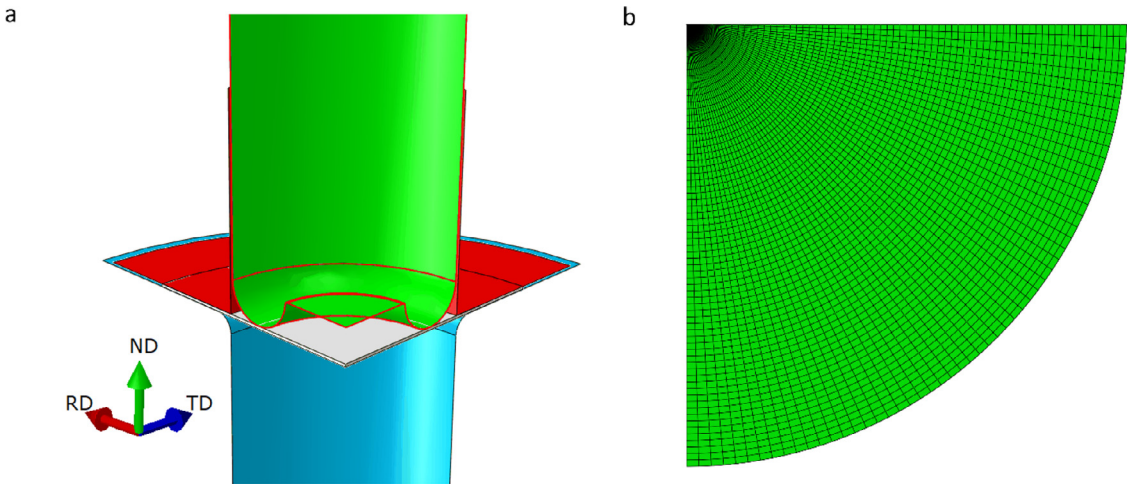

Fig. 4. (a) Simulation setup and (b) mesh representing the blank for deep drawing of a cup.

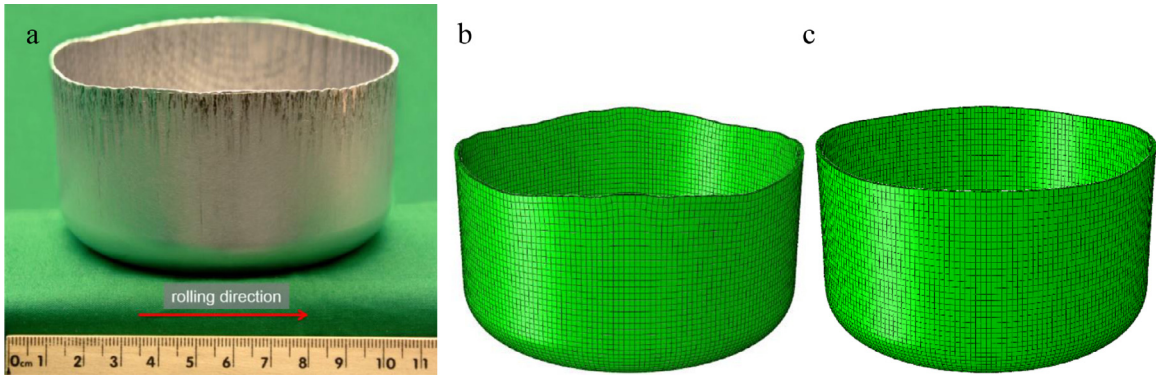

Fig. 6. (a) A photo of the formed cup (Tian et al., 2017). Predictions using (b) FE-EPSC and (c) HAH.

response to a response of a polycrystalline aggregate, which is then embedded et each finite element integration point as a constitutive law to simulate part-level macroscopic behavior. The latter model is an anisotropic yield function incorporating distortional hardening using the homogeneous anisotropic hardening (HAH_{20}) approach also embedded in implicit finite elements. While the EPSC model accounts for the evolution of microstructure and deformation mechanisms operating at the grain level, the macro model is capable of representing these effects in a less explicit way. The work experimentally verified both models embedded in finite elements. Parameters pertaining to the models are identified using a set of monotonic and cyclic tests performed for AA6022-T4. The models are verified by predicting data for R-value and the yield surfaces. The adjusted models are then used within the FEM software Abaqus to simulate deep drawing of a cylindrical cup. Both formulations achieve acceptable accuracy in terms of simulating geometrical changes of the cup during forming. In particular, the models predict experimentally measured force versus displacement, cup height, and cup thinning with good accuracy.

The work has shown that both models can be used to predict phenomena pertaining to the behavior of alloy AA6022-T4. Moreover, the models can predict geometrical changes important for optimization of the sheet metal forming processes. The overall computational time involved in the simulations is presented in Table 5. The FE-EPSC model is regarded as accurate and easy to adjust but also as computationally intensive. In contrast, the HAH_{20} model is fast but more involved requiring more mechanical tests to adjust the parameters for a given

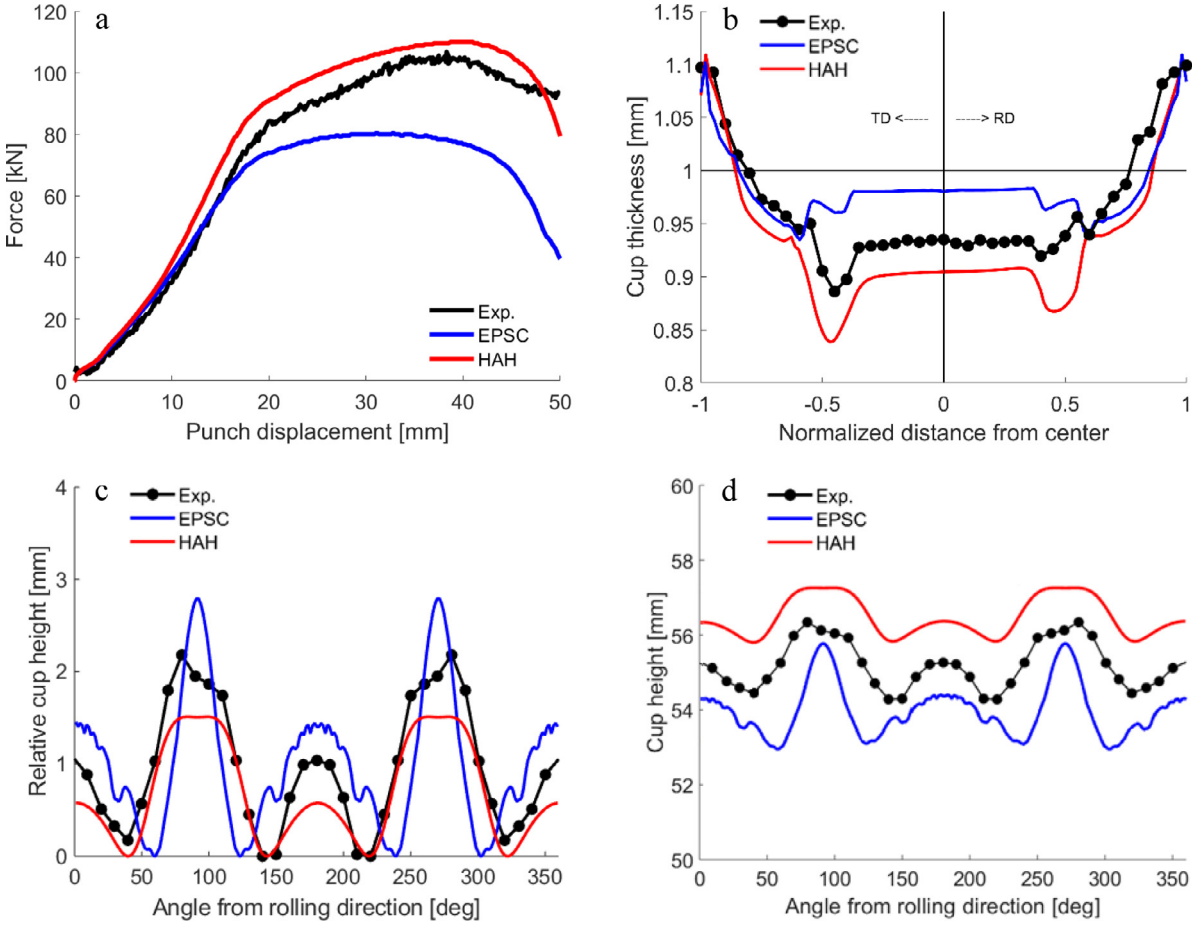

Fig. 7. Comparison of measured and simulated: (a) punch load versus punch displacement curve during drawing, (b) change in sheet thickness after drawing in TD and RD, (c) relative cup height with the lowest/minimum point set to zero, and (d) actual cup height. The simulations are based on the soft contact conditions.

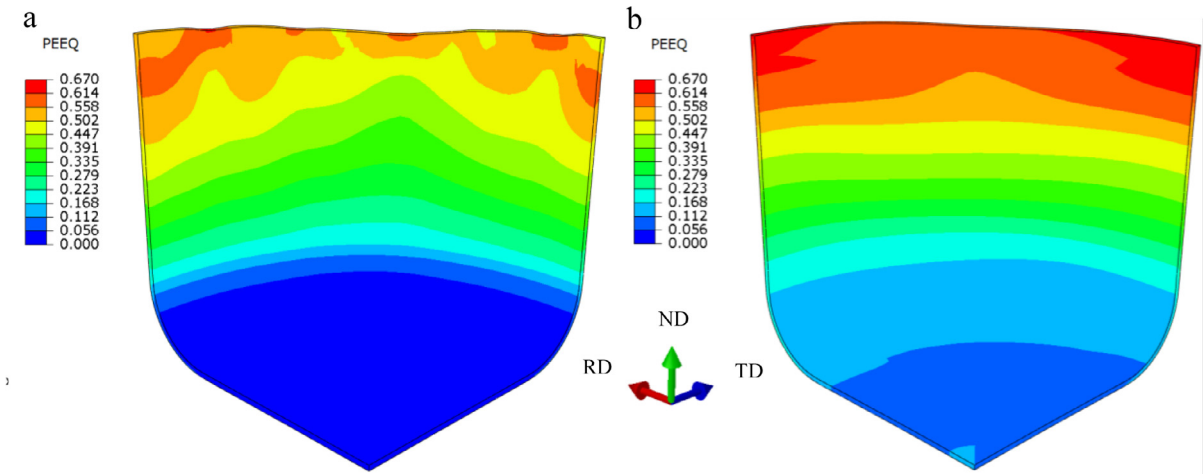

Fig. 8. Equivalent plastic strain (PEEQ) fields predicted by (a) FE-EPSC and (b) HAH models.

material. Future work will explore computational schemes and platforms to accelerate the EPSC model (Kalidindi et al., 2006; Knezevic et al., 2009; Knezevic and Kalidindi, 2007, 2008; Knezevic and Savage, 2014; Mihaila et al., 2014; Savage and Knezevic, 2015).

Table 5
Computational time involved in the simulation using FE-EPSC and HAH. The jobs were run on a computer workstation Intel® Xenon® Gold 6130 CPU @ 2.10 GHz with system memory of 192 GB using parallel processing with 20 CPUs.

	EPSC	HAH
Wall clock time in hours: minutes	127: 47	10: 26

6. Conclusions

In this paper, we presented a comparative study between micro- and

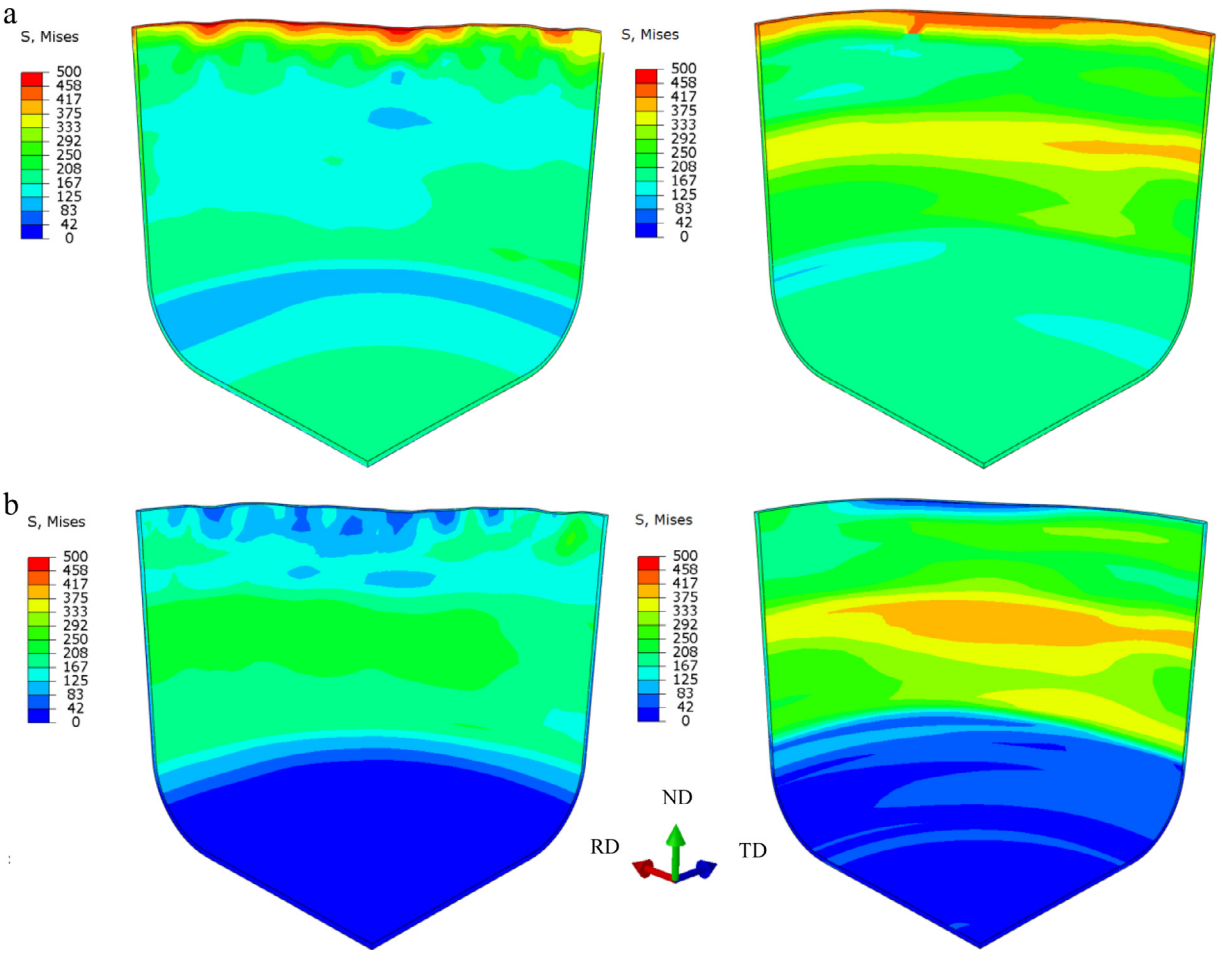

Fig. 9. Von Mises stress fields predicted using FE-EPSC on the left and HAH on the right (a) before springback and (b) after springback.

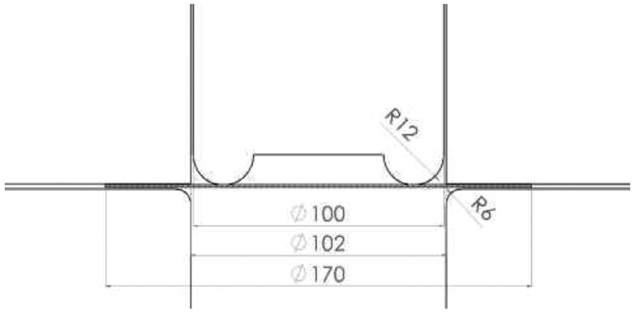

Fig. A1. Solidworks drawing showing the setup for cup drawing (units are in mm). The cup drawing was performed from a 170 mm diameter cylindrical blank of 1 mm in thickness. The punch was 100 mm in diameter, with a 12 mm radius, while the die opening was 102 mm, with a 6 mm die radius.

macro-mechanical constitutive models in predicting mechanical behavior of the AA6022-T4 sheet. The micro model is a recently developed implicit formulation of EPSC, which is coupled with the implicit finite elements. In the coupled formulation, every finite element integration point embeds the implicit EPSC constitutive law that accounts for the directionality of deformation mechanisms and microstructural evolution. The crystallography based EPSC model integrates a dislocation-based hardening law and accounts for inter-granular stresses and slip system level back-stresses, which make it capable of capturing non-linear unloading and the Bauschinger effect. The macro model is a recently developed anisotropic yield function incorporating distortional hardening using the HAH approach. Parameters pertaining to the micro and macro models are identified using experimental data from a set of monotonic and cyclic tests performed on a AA6022-T4 sheet sample. Data of increasing complexity such as R-value and anisotropic yield surfaces are then used to verify the models. Finally, geometrical changes including the earing profile and sheet thinning/thickening during drawing predicted using the two constitutive formulations are used to further evaluate the predictive characteristics of the models. It is demonstrated that both models are capable of capturing non-linear unloading, the BE, and anisotropy in hardening rates as well as the directionally dependent cup height and thinning/thickening of the sheet in drawing. The FE-EPSC model is regarded as easy to adjust but also as computationally intensive. In contrast, the HAH_{20} model is fast but more involved to adjust for a given material.

CRediT authorship contribution statement

Zhangxi Feng: Formal analysis, Investigation, Software, Validation, Visualization, Writing - review & editing. **Seong-Yong Yoon:** Formal analysis, Investigation, Software, Validation, Visualization, Writing - review & editing. **Jae-Hyun Choi:** Formal analysis, Investigation, Software, Validation, Visualization. **Timothy J. Barrett:** Formal analysis, Investigation, Software, Validation, Visualization. **Milovan Zecevic:** Formal analysis, Investigation, Software, Validation, Visualization. **Frederic Barlat:** Conceptualization, Funding acquisition, Methodology, Project administration, Resources, Supervision, Writing - review & editing. **Marko Knezevic:** Conceptualization, Funding acquisition, Methodology, Project administration, Resources, Supervision, Writing - original draft, Writing - review & editing.

Declaration of Competing Interest

The authors declare that they have no known competing financial interests or personal relationships that could have appeared to influence the work reported in this paper.

Acknowledgments

Z. F., T. J. B, M. Z., and M. K. acknowledge support by the U.S. National Science Foundation under the Grant No. CMMI-1650641. S.Y.Y., J.H.C. and F.B. are grateful to POSCO for generous financial support.

Supplementary materials

Supplementary material associated with this article can be found, in the online version, at doi:10.1016/j.mechmat.2020.103422.

Appendix A

Fig. A1.

References

Alcoa, Alloy 6022 Sheet, North American Rolled Products.
Ardeljan, M., Knezevic, M., 2018. Explicit modeling of double twinning in AZ31 using crystal plasticity finite elements for predicting the mechanical fields for twin variant selection and fracture analyses. Acta. Mater. 157, 339–354.
Barlat, F., Aretz, H., Yoon, J.W., Karabin, M., Brem, J., Dick, R., 2005. Linear transformation-based anisotropic yield functions. Int. J. Plast. 21, 1009–1039.
Barlat, F., Glazov, M., Brem, J., Lege, D., 2002. A simple model for dislocation behavior, strain and strain rate hardening evolution in deforming aluminum alloys. Int. J. Plast. 18, 919–939.
Barlat, F., Gracio, J.J., Lee, M.-G., Rauch, E.F., Vincze, G., 2011. An alternative to kinematic hardening in classical plasticity. Int. J. Plast. 27, 1309–1327.
Barlat, F., Yoon, S.Y., Lee, S.Y., Kim, J.H., 2020. Distortional plasticity framework with application to advanced high strength steel. Int J Solids Struct.
Barrett, T.J., Eghtesad, A., McCabe, R.J., Clausen, B., Brown, D.W., Vogel, S.C., Knezevic, M., 2019. A generalized spherical harmonics-based procedure for the interpolation of partial datasets of orientation distributions to enable crystal mechanics-based simulations. Materialia 6, 100328.
Barrett, T.J., Knezevic, M., 2019. Deep drawing simulations using the finite element method embedding a multi-level crystal plasticity constitutive law: experimental verification and sensitivity analysis. Comput Methods Appl Mech Eng 354, 245–270.
Barrett, T.J., Knezevic, M., 2020. Modeling material behavior during continuous bending under tension for inferring the post-necking strain hardening response of ductile sheet metals: application to DP 780 steel. Int. J. Mech. Sci. 174, 105508.
Bathe, K.-J., 1996. Finite Element Procedures. Prentice Hall, Englewood Cliffs, N.J.
Bauschinger, J., 1886. Über die Veränderung der Elasticitätsgrenze und Festigkeit des Eisen und Stahls durch Strecken und Quetschen, durch Erwarmen und Abkühlen und durch oftmal wiederholte Beanspruchung. Mitteilungen aus dem mechanisch-

technischen Laboratorium der k. polytechnischen Schule, 1877–1836.
Bayley, C.J., Brekelmans, W.A.M., Geers, M.G.D., 2006. A comparison of dislocation induced back stress formulations in strain gradient crystal plasticity. Int. J. Solids Struct. 43, 7268–7286.
Beyerlein, I.J., Tomé, C.N., 2007. Modeling transients in the mechanical response of copper due to strain path changes. Int. J. Plast. 23, 640–664.
Beyerlein, I.J., Tomé, C.N., 2008. A dislocation-based constitutive law for pure Zr including temperature effects. Int. J. Plast. 24, 867–895.
Cantara, A.M., Zecevic, M., Eghtesad, A., Poulin, C.M., Knezevic, M., 2019. Predicting elastic anisotropy of dual-phase steels based on crystal mechanics and microstructure. Int. J. Mech. Sci. 151, 639–649.
Eghtesad, A., Barrett, T.J., Knezevic, M., 2018. Compact reconstruction of orientation distributions using generalized spherical harmonics to advance large-scale crystal plasticity modeling: verification using cubic, hexagonal, and orthorhombic polycrystals. Acta. Mater. 155, 418–432.
Eghtesad, A., Knezevic, M., 2020. High-performance full-field crystal plasticity with dislocation-based hardening and slip system back-stress laws: application to modeling deformation of dual-phase steels. J. Mech. Phys. Solids 134, 103750.
Engler, O., Hirsch, J., 2002. Texture control by thermomechanical processing of AA6xxx Al–Mg–Si sheet alloys for automotive applications—A review. Mater. Sci. Eng. A 336, 249–262.
Eshelby, J.D., 1957. The determination of the elastic field of an ellipsoidal inclusion, and related problems. Proc R. Soc. Lond. A 241, 376–396.
Eskin, D.G., Kharakterova, M.L., 2001. The effect of silicon and copper on the precipitation hardnening of sheets of 6xxx series alloy. Mater. Technol. 35, 5–8.
Fleck, N.A., Muller, G.M., Ashby, M.F., Hutchinson, J.W., 1994. Strain gradient plasticity: theory and experiment. Acta Metallurgica et Materialia 42, 475–487.
Franciosi, P., Zaoui, A., 1982. Multislip in f.c.c. crystals a theoretical approach compared with experimental data. Acta Metallurgica 30, 1627–1637.
Ghorbanpour, S., Alam, M.E., Ferreri, N.C., Kumar, A., McWilliams, B.A., Vogel, S.C., Bicknell, J., Beyerlein, I.J., Knezevic, M., 2020. Experimental characterization and crystal plasticity modeling of anisotropy, tension-compression asymmetry, and texture evolution of additively manufactured Inconel 718 at room and elevated temperatures. Int. J. Plast. 125, 63–79.
Ghorbanpour, S., Zecevic, M., Kumar, A., Jahedi, M., Bicknell, J., Jorgensen, L., Beyerlein, I.J., Knezevic, M., 2017. A crystal plasticity model incorporating the effects of precipitates in superalloys: application to tensile, compressive, and cyclic deformation of Inconel 718. Int. J. Plast. 99, 162–185.
Ghosh, M., Miroux, A., Kestens, L., 2015. Correlating r-value and through thickness texture in Al–Mg–Si alloy sheets. J. Alloys Compd. 619, 585–591.
Harder, J., 1999. A crystallographic model for the study of local deformation processes in polycrystals. Int. J. Plasticity 15, 605–624.
Hasegawa, T., Yakou, T., Karashima, S., 1975. Deformation behaviour and dislocation structures upon stress reversal in polycrystalline aluminium. Mater. Sci. Eng. 20, 267–276.
Henn, P., Liewald, M., Sindel, M., 2017. Characterising ductility of 6xxx-series aluminium sheet alloys at combined loading conditions. In: AIP Conference Proceedings. 1896, 020008.
Hirsch, J., 2014. Recent development in aluminium for automotive applications. Trans. Nonferrous Metals Soc. China 24, 1995–2002.
Hirsch, J., Al-Samman, T., 2013. Superior light metals by texture engineering: optimized aluminum and magnesium alloys for automotive applications. Acta. Mater. 61, 818–843.
Hockett, J.E., Sherby, O.D., 1975. Large strain deformation of polycrystalline metals at low homologous temperatures. J. Mech. Phys. Solids 23, 87–98.
Hosford, W.F., Caddell, R.M., 2011. Metal forming: Mechanics and Metallurgy. Cambridge University Press, New York, USA.
Jaafar, A., Rahmat, A., Zainol, l., Hussain, Z., 2012. Effects of Composition on the Mechanical Properties and Microstructural Development of Dilute 6000 Series Alloys. Journal of Applied Science 12, 775–780.
Jahedi, M., Knezevic, M., Paydar, M., 2015. High-Pressure Double Torsion as a Severe Plastic Deformation Process: experimental Procedure and Finite Element Modeling. J. Mater. Eng. Perform. 24, 1471–1482.
Kalidindi, S.R., Duvvuru, H.K., Knezevic, M., 2006. Spectral calibration of crystal plasticity models. Acta. Mater. 54, 1795–1804.
Kassner, M.E., Geantil, P., Levine, L.E., 2013. Long range internal stresses in single-phase crystalline materials. Int. J. Plasticity 45, 44–60.
Khadyko, M., Dumoulin, S., Cailletaud, G., Hopperstad, O.S., 2016. Latent hardening and plastic anisotropy evolution in AA6060 aluminium alloy. Int. J. Plast. 76, 51–74.
Kitayama, K., Tomé, C.N., Rauch, E.F., Gracio, J.J., Barlat, F., 2013. A crystallographic dislocation model for describing hardening of polycrystals during strain path changes. Application to low carbon steels. Int. J. Plasticity 46, 54–69.
Knezevic, M., Al-Harbi, H.F., Kalidindi, S.R., 2009. Crystal plasticity simulations using discrete Fourier transforms. Acta. Mater. 57, 1777–1784.
Knezevic, M., Beyerlein, I.J., Brown, D.W., Sisneros, T.A., Tomé, C.N., 2013a. A polycrystal plasticity model for predicting mechanical response and texture evolution during strain-path changes: application to beryllium. Int. J. Plast. 49, 185–198.
Knezevic, M., Beyerlein, I.J., Lovato, M.L., Tomé, C.N., Richards, A.W., McCabe, R.J., 2014. A strain-rate and temperature dependent constitutive model for BCC metals incorporating non-Schmid effects: application to tantalum–tungsten alloys. Int. J. Plast. 62, 93–104.
Knezevic, M., Kalidindi, S.R., 2007. Fast computation of first-order elastic-plastic closures for polycrystalline cubic-orthorhombic microstructures. Comput. Mater. Sci. 39, 643–648.
Knezevic, M., Kalidindi, S.R., Fullwood, D., 2008. Computationally efficient database and spectral interpolation for fully plastic Taylor-type crystal plasticity calculations of face-centered cubic polycrystals. Int. J. Plast. 24, 1264–1276.
Knezevic, M., Landry, N.W., 2015. Procedures for reducing large datasets of crystal orientations using generalized spherical harmonics. Mech. Mater. 88, 73–86.
Knezevic, M., Lebensohn, R.A., Cazacu, O., Revil-Baudard, B., Proust, G., Vogel, S.C., Nixon, M.E., 2013b. Modeling bending of α-titanium with embedded polycrystal plasticity in implicit finite elements. Mater. Sci. Eng. A 564, 116–126.
Knezevic, M., McCabe, R.J., Lebensohn, R.A., Tomé, C.N., Liu, C., Lovato, M.L., Mihaila, B., 2013c. Integration of self-consistent polycrystal plasticity with dislocation density based hardening laws within an implicit finite element framework: application to low-symmetry metals. J. Mech. Phys. Solids 61, 2034–2046.
Knezevic, M., Savage, D.J., 2014. A high-performance computational framework for fast crystal plasticity simulations. Comput. Mater. Sci. 83, 101–106.
Knockaert, R., Chastel, Y., Massoni, E., 2000. Rate-independent crystalline and polycrystalline plasticity, application to FCC materials. Int. J. Plasticity 16, 179–198.
Kocks, U.F., Brown, T.J., 1966. Latent hardening in aluminum. Acta Metall 14, 87–98.
Kocks, U.F., Franciosi, P., Kawai, M., 1991. A forest model of latent hardening and its application to polycrystal deformations. Textures Microstruct. 14, 1103–1114.
Lavrentev, F.F., 1980. The type of dislocation interaction as the factor determining work hardening. Mater. Sci. Eng. 46, 191–208.
Li, K., Carden, W., Wagoner, R., 2002. Simulation of springback. Int. J. Mech. Sci. 44, 103–122.
Lipinski, P., Berveiller, M., 1989. Elastoplasticity of micro-inhomogeneous metals at large strains. Int. J. Plast. 5, 149–172.
Mecking, H., Kocks, U.F., 1981. Kinetics of flow and strain-hardening. Acta Metall. Mater. 29, 1865–1875.
Miao, W.F., Laughlin, D.E., 1999. Precipitation hardening in aluminum alloy 6022. Scr. Mater. 40, 873–878.
Mihaila, B., Knezevic, M., Cardenas, A., 2014. Three orders of magnitude improved efficiency with high-performance spectral crystal plasticity on GPU platforms. Int. J. Numer. Methods Eng. 97, 785–798.
Miller, W.S., Zhuang, L., Bottema, J., Wittebrood, A.J., De Smet, P., Haszler, A., Vieregge, A., 2000. Recent development in aluminium alloys for the automotive industry. Mater. Sci. Eng. A 280, 37–49.
Mughrabi, H., 1983. Dislocation wall and cell structures and long-range internal stresses in deformed metal crystals. Acta Metall 31, 1367–1379.
Nagtegaal, J.C., Veldpaus, F.E., 1984. On the implementation of finite strain plasticity equations in a numerical model. Numer. Methods Ind. Form. Process. 351–371.
Neil, C.J., Wollmershauser, J.A., Clausen, B., Tomé, C.N., Agnew, S.R., 2010. Modeling lattice strain evolution at finite strains and experimental verification for copper and stainless steel using in situ neutron diffraction. Int. J. Plast. 26, 1772–1791.
Poulin, C.M., Barrett, T.J., Knezevic, M., 2019a. Inferring post-necking strain hardening behavior of sheets by a combination of continuous bending under tension testing and finite element modeling. Exp. Mech.
Poulin, C.M., Korkolis, Y.P., Kinsey, B.L., Knezevic, M., 2019b. Over five-times improved elongation-to-fracture of dual-phase 1180 steel by continuous-bending-under-tension. Mater. Des. 161, 95–105.
Rabahallah, M., Bouvier, S., Balan, T., Bacroix, B., 2009. Numerical simulation of sheet metal forming using anisotropic strain-rate potentials. Mater. Sci. Eng. A 517, 261–275.
Richmond, O., Spitzig, W., 1980. Pressure dependence and dilatancy of plastic flow. Theoret. Appl. Mech. 377–386.
Savage, D.J., Knezevic, M., 2015. Computer implementations of iterative and non-iterative crystal plasticity solvers on high performance graphics hardware. Comput. Mech. 56, 677–690.
Spitzig, W.A., Sober, R.J., Richmond, O., 1975. Pressure dependence of yielding and associated volume expansion in tempered martensite. Acta Metall 23, 885–893.
Teodosiu, C., Raphanel, J.L., 1991. Finite element simulations of large elastoplastic deformations of multicrystals. Proc. Int. Sem. MECAMAT 91, 153–168.
Tian, H., Brownell, B., Baral, M., Korkolis, Y.P., 2017. Earing in cup-drawing of anisotropic Al-6022-T4 sheets. Int. J. Mater. Form. 10, 329–343.
Turner, P.A., Tomé, C.N., 1994. A study of residual stresses in Zircaloy-2 with rod texture. Acta Metall. Mater. 42, 4143–4153.
van den Boogaard, T., Havinga, J., Belin, A., Barlat, F., 2016. Parameter reduction for the Yld2004-18p yield criterion. Int. J. Mater. Form. 9, 175–178.
Wagoner, R.H., Lim, H., Lee, M.-.G., 2013. Advanced Issues in springback. Int. J. Plasticity 45, 3–20.
Wen, W., Borodachenkova, M., Tomé, C.N., Vincze, G., Rauch, E.F., Barlat, F., Grácio, J.J., 2015. Mechanical behavior of Mg subjected to strain path changes: experiments and modeling. Int. J. Plasticity 73, 171–183.
Withers, P.J., Bhadeshia, H.K.D.H., 2001. Residual stress. Part 1 – Measurement techniques. Mater. Sci. Technol. 17, 355–365.
Wollmershauser, J.A., Clausen, B., Agnew, S.R., 2012. A slip system-based kinematic hardening model application to in situ neutron diffraction of cyclic deformation of austenitic stainless steel. Int. J. Fatigue 36, 181–193.
Yoon, J.W., Barlat, F., Dick, R.E., Karabin, M.E., 2006. Prediction of six or eight ears in a drawn cup based on a new anisotropic yield function. Int. J. Plast. 22, 174–193.
Yoon, J.W., Barlat, F., Gracio, J.J., Rauch, E., 2005. Anisotropic strain hardening behavior in simple shear for cube textured aluminum alloy sheets. Int. J. Plast. 21, 2426–2447.
Yoon, S.Y., Lee, S.Y., Barlat, F., 2020. Numerical integration algorithm of updated homogeneous anisotropic hardening model in finite element framework. Comput. Methods Appl. Mech. Eng.
Zare, H., Jahedi, M., Toroghinejad, M.R., Meratian, M., Knezevic, M., 2016. Compressive, shear, and fracture behavior of CNT reinforced Al matrix composites manufactured by severe plastic deformation. Mater. Des. 106, 112–119.
Zarei, H., 2008. Experimental and Numerical Investigation of Crash Structures Using Aluminum Alloys. Cuvillier Verlag, Göttingen, Germany.

Zecevic, M., Beyerlein, I.J., Knezevic, M., 2017. Coupling elasto-plastic self-consistent crystal plasticity and implicit finite elements: applications to compression, cyclic tension-compression, and bending to large strains. Int. J. Plast. 93, 187–211.
Zecevic, M., Knezevic, M., 2015. A dislocation density based elasto-plastic self-consistent model for the prediction of cyclic deformation: application to Al6022-T4. Int. J. Plast. 72, 200–217.
Zecevic, M., Knezevic, M., 2017. Modeling of sheet metal forming based on implicit embedding of the elasto-plastic self-consistent formulation in shell elements: application to cup drawing of AA6022-T4. JOM 69, 922–929.
Zecevic, M., Knezevic, M., 2018a. Latent hardening within the elasto-plastic self-consistent polycrystal homogenization to enable the prediction of anisotropy of AA6022-T4 sheets. Int. J. Plast. 105, 141–163.
Zecevic, M., Knezevic, M., 2018b. A new visco-plastic self-consistent formulation implicit in dislocation-based hardening within implicit finite elements: application to high strain rate and impact deformation of tantalum. Comput. Methods Appl. Mech. Eng. 341, 888–916.
Zecevic, M., Knezevic, M., 2019. An implicit formulation of the elasto-plastic self-consistent polycrystal plasticity model and its implementation in implicit finite elements. Mech. Mater. 136, 103065.
Zecevic, M., Knezevic, M., Beyerlein, I.J., McCabe, R.J., 2016a. Texture formation in orthorhombic alpha-uranium under simple compression and rolling to high strains. J. Nuclear Mater. 473, 143–156.
Zecevic, M., Knezevic, M., Beyerlein, I.J., Tomé, C.N., 2015. An elasto-plastic self-consistent model with hardening based on dislocation density, twinning and de-twinning: application to strain path changes in HCP metals. Mater. Sci. Eng. A 638, 262–274.
Zecevic, M., Korkolis, Y.P., Kuwabara, T., Knezevic, M., 2016b. Dual-phase steel sheets under cyclic tension–compression to large strains: experiments and crystal plasticity modeling. J. Mech. Phys. Solids 96, 65–87.
Zecevic, M., Roemer, T., Knezevic, M., Korkolis, Y., Kinsey, B., 2016c. Residual Ductility and Microstructural Evolution in Continuous-Bending-under-Tension of AA-6022-T4. Materials (Basel) 9, 130.
Zecevic, M., Upadhyay, M.V., Polatidis, E., Panzner, T., Van Swygenhoven, H., Knezevic, M., 2019. A crystallographic extension to the Olson-Cohen model for predicting strain path dependence of martensitic transformation. Acta. Mater. 166, 386–401.